

Electronic Supplementary Information

Cerium-induced lattice disordering in Co-based nanocatalysts promoting the hydrazine electro-oxidation behavior

Jiechen Li,[†] Changgang Dong,[†] Min Guo, Wen Gao, Luyao Kang, Fengcai Lei, Pin Hao, Junfeng Xie* and Bo Tang*

College of Chemistry, Chemical Engineering and Materials Science, Key Laboratory of Molecular and Nano Probes (Ministry of Education), Collaborative Innovation Center of Functionalized Probes for Chemical Imaging in Universities of Shandong, Institute of Molecular and Nano Science, Shandong Normal University, Jinan, Shandong, 250014, P. R. China. E-mail: xiejf@sdu.edu.cn; tangb@sdu.edu.cn.

[†] These authors contributed equally to this work.

1. Experimental section

1.1 Synthesis of the pristine and Ce-incorporated ZIF-67 and Co-N-C

Typically, $\text{Co}(\text{NO}_3)_2 \cdot 6\text{H}_2\text{O}$ and $\text{CeCl}_3 \cdot 7\text{H}_2\text{O}$ with total amount of 3 mmol were dissolved in 30 mL methanol, and 12 mmol 2-methylimidazole (2-MeIm) was dissolved in 10 mL methanol. Then, the solution of 2-MeIm was subsequently injected into the solution of metal salts. After stirring at room temperature for 24 h, purple precipitates were collected by centrifugation, washed with methanol for several times and dried at 40 °C under vacuum. By simply controlling the content of the metal salts, pristine and Ce-incorporated ZIF-67 can be obtained. The as-obtained ZIF-67 precursors were heated to 650 °C in a tube furnace at a heating rate of 5 °C min⁻¹ under Ar atmosphere and maintained for 2 h to obtain the pristine and Ce-incorporated Co-N-C.

1.2 Structural characterizations

The X-ray diffraction (XRD) was performed on a Philips X'Pert Pro Super diffractometer with Cu K α radiation ($\lambda = 1.54178 \text{ \AA}$). The Raman spectroscopy was performed with a laser micro-Raman spectrometer (Horiba LabRAM HR Evolution, 532 nm excitation wavelength). The scanning electron microscopy (SEM) images were taken on a JEOL JSM-6700F SEM. The transmission electron microscopy (TEM) was carried out on a JEM-2100F field emission electron microscope at an acceleration voltage of 200 kV. The high-resolution TEM (HRTEM), high-angle annular dark-field scanning transmission electron microscopy (HAADF-STEM) and corresponding elemental mapping analyses were performed on a ThermoFischer Talos F200X TEM. The nitrogen adsorption-desorption isotherms were carried out by using a Micromeritics ASAP 2460 system, and all the gas adsorption experiments were performed at liquid-nitrogen temperature (77 K) after degassed at 300 °C for 6 h. The Ce/(Ce+Co) values were determined by the inductively coupled plasma optical emission spectrum (ICP-OES) on a Perkin Elmer Optima 7300DV ICP emission spectroscope. The X-ray photoelectron spectroscopy (XPS) were performed on a VGESCALAB MKII X-ray photoelectron spectrometer with an excitation source of Mg K α = 1253.6 eV, and the

resolution level was lower than 1 atom%.

1.3 Electrocatalytic study

All the electrochemical measurements for investigating were conducted using a three-electrode system on an electrochemical workstation (Ivium Vertex. C. EIS) at room temperature. All of the potentials were calibrated to a reversible hydrogen electrode (RHE). Typically, 4 mg of catalyst and 50 μL Nafion solution (Sigma Aldrich, 5 wt%) were dispersed in 1 mL isopropanol by sonicating for at least 30 min to form a homogeneous ink. Then 20 μL of the dispersion (containing 80 μg of catalyst) was loaded onto a glassy carbon electrode with 3 mm diameter, leading to a catalyst loading of 1.14 mg cm^{-2} . The as-prepared catalyst film was allowed to be dried at room temperature. Cyclic voltammetry (CV) and linear sweep voltammetry (LSV) with a scan rate of 5 mV s^{-1} were conducted in the electrolyte containing 0.1 M KOH and 0.1 M hydrazine without being purged with N_2 (the result is not affected by the aeration of N_2). A Hg/HgO electrode was used as the reference electrode, a platinum gauze electrode (2 \times 2 cm, 60 mesh) was used as the counter electrode. The electrochemical impedance spectroscopy (EIS) measurements were conducted at 0.45 V vs. RHE with frequencies from 10^{-2} to 10^{-5} Hz.

2. Additional physical and electrochemical characterizations

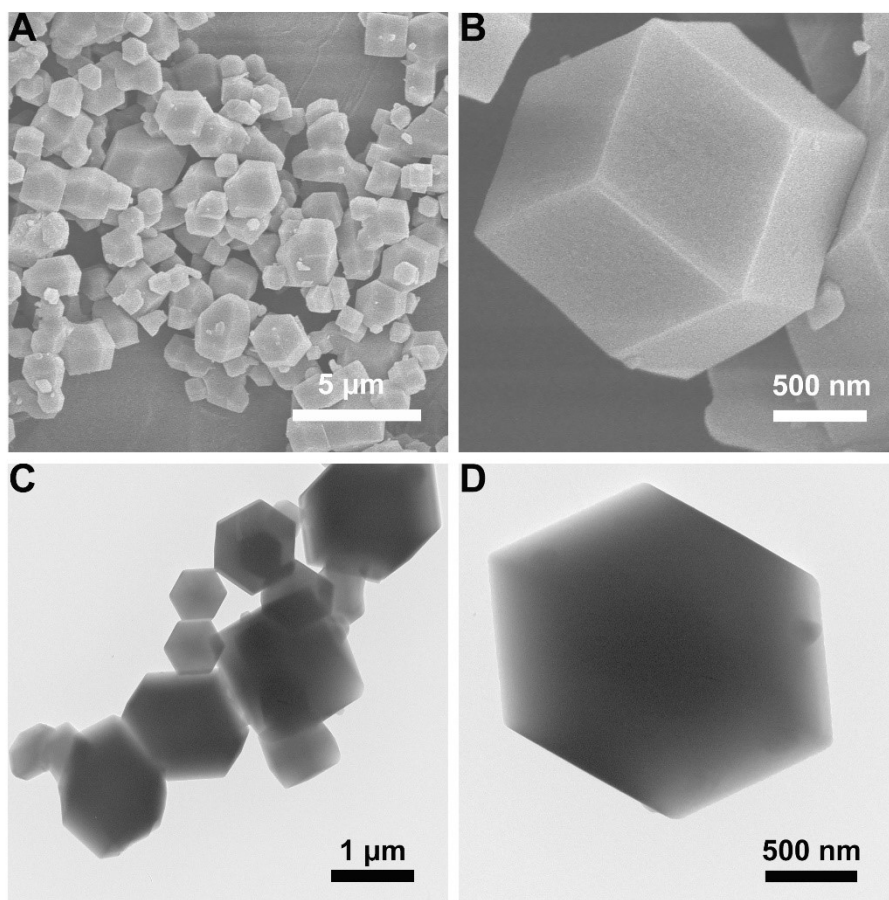


Fig. S1 (A-B) SEM and (C-D) TEM images of the pristine ZIF-67 without Ce incorporation.

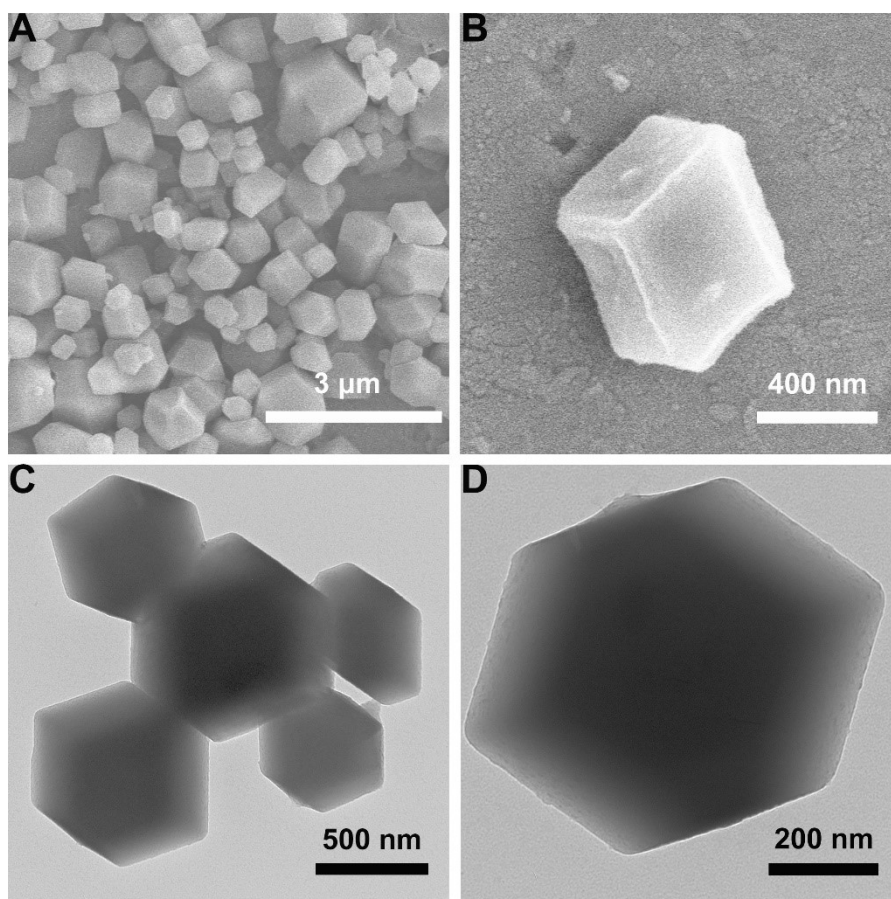


Fig. S2 (A-B) SEM and (C-D) TEM images of ZIF-67 with 1% Ce incorporation.

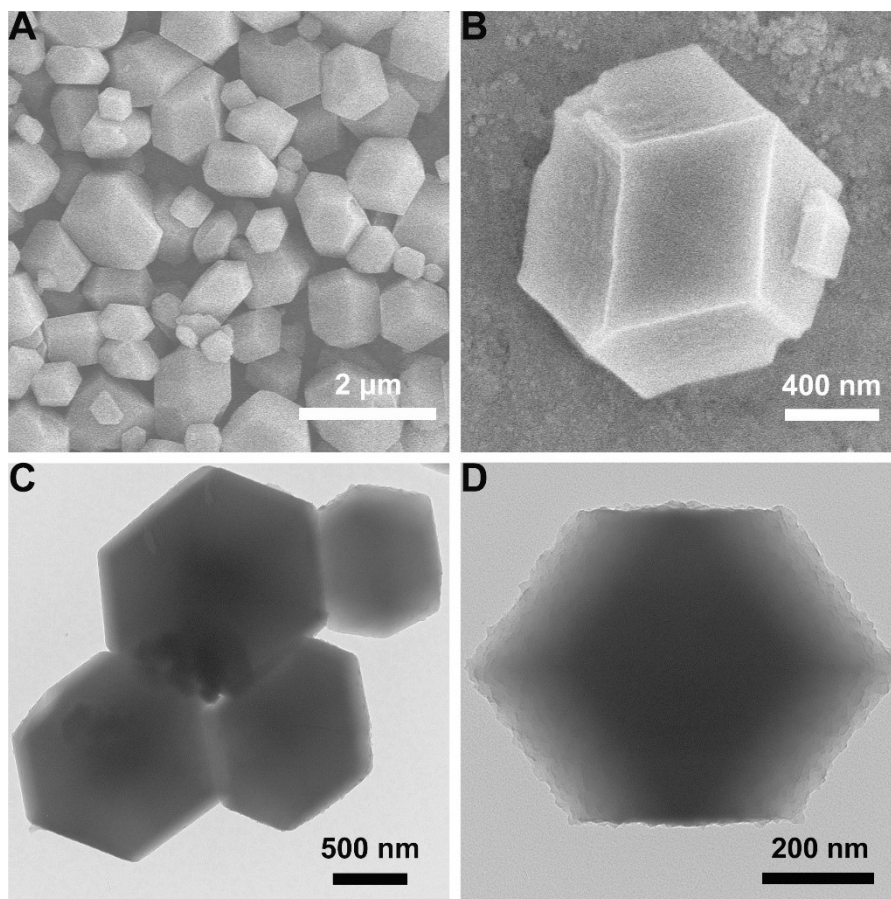


Fig. S3 (A-B) SEM and (C-D) TEM images of ZIF-67 with 3% Ce incorporation.

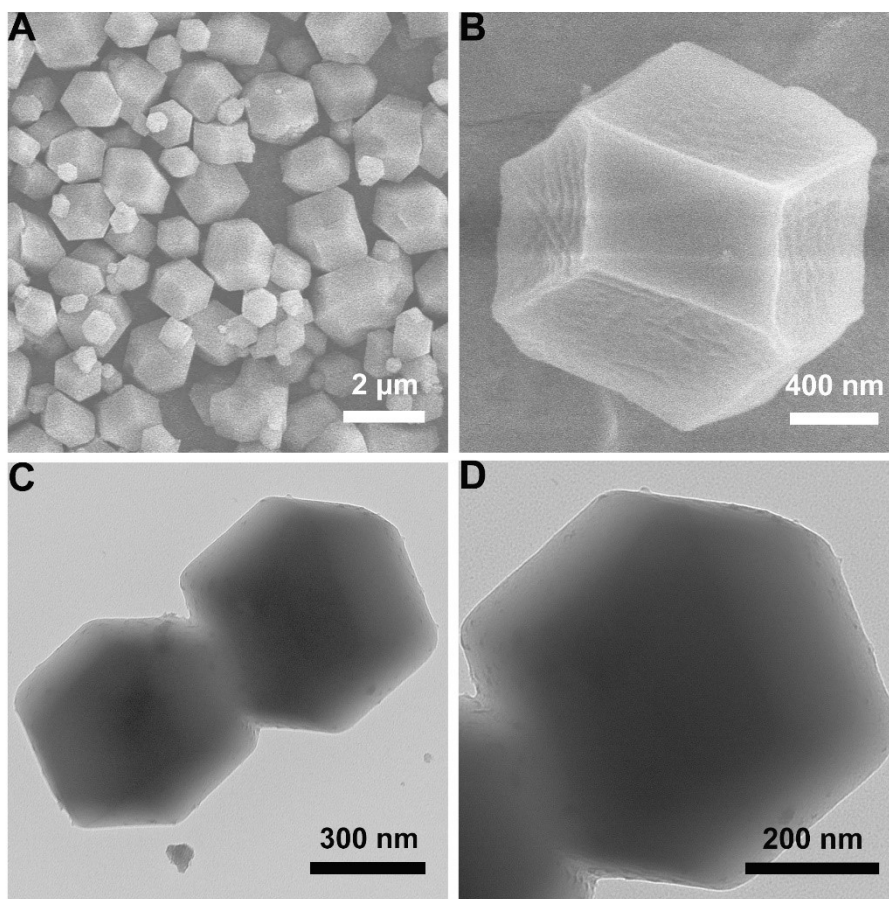


Fig. S4 (A-B) SEM and (C-D) TEM images of ZIF-67 with 5% Ce incorporation.

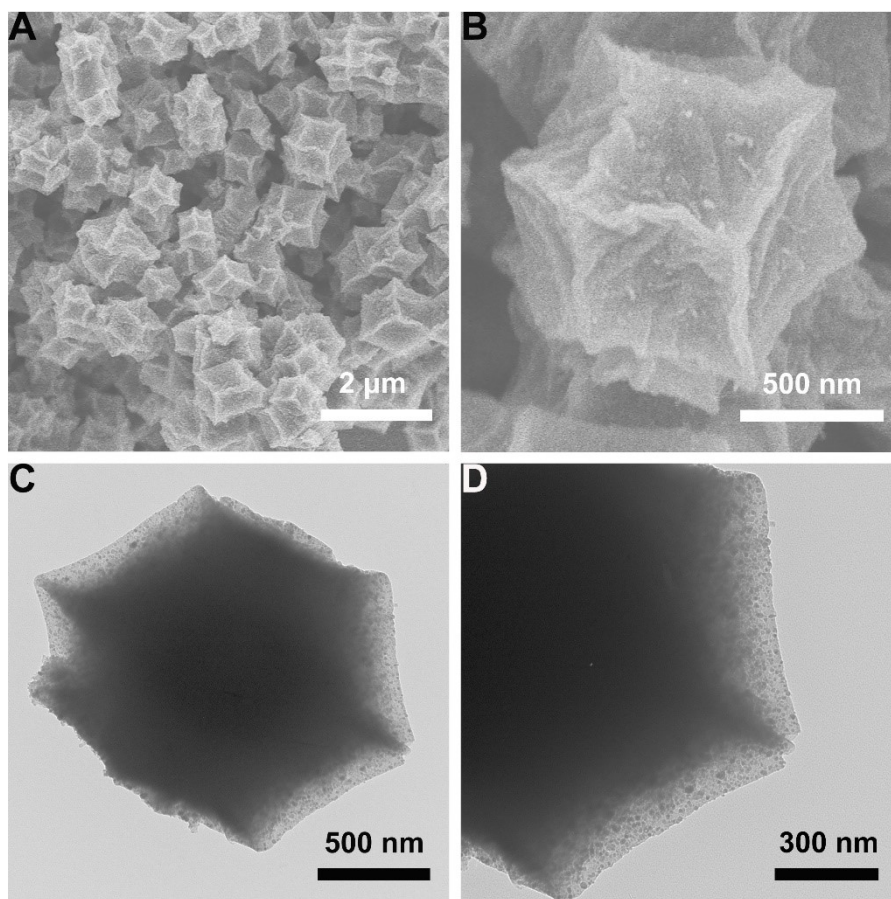


Fig. S5 (A-B) SEM and (C-D) TEM images of the pristine Co-N-C without Ce incorporation.

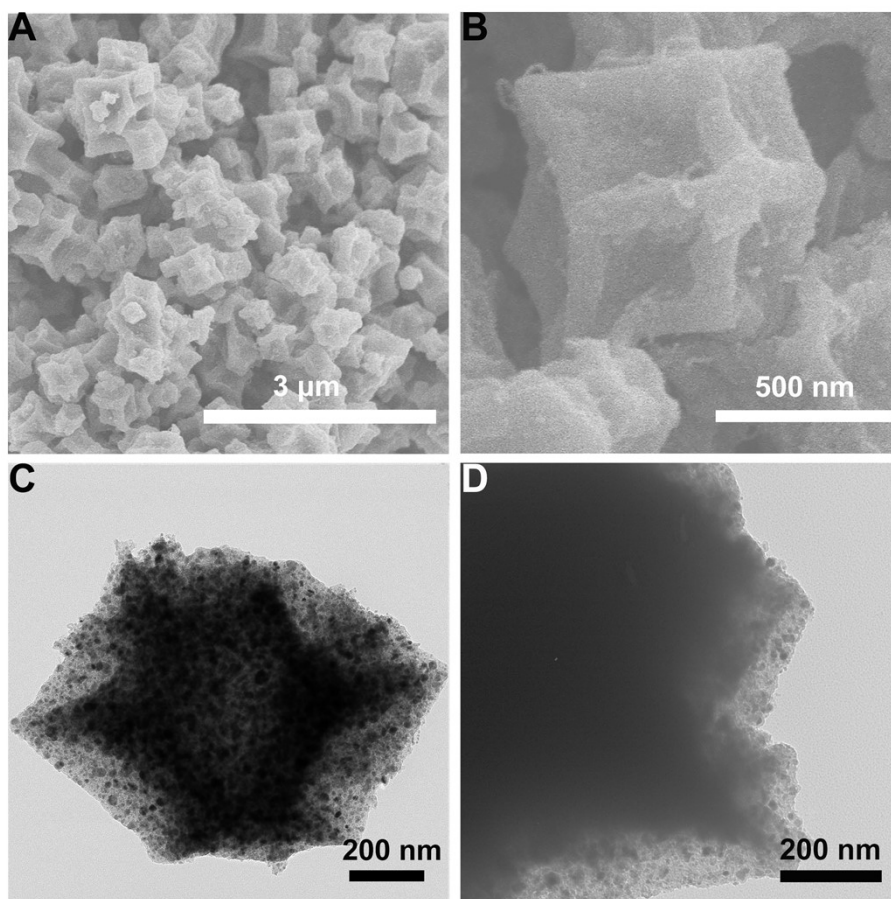


Fig. S6 Additional SEM (A) and TEM (B) images of 1%Ce:Co-N-C.

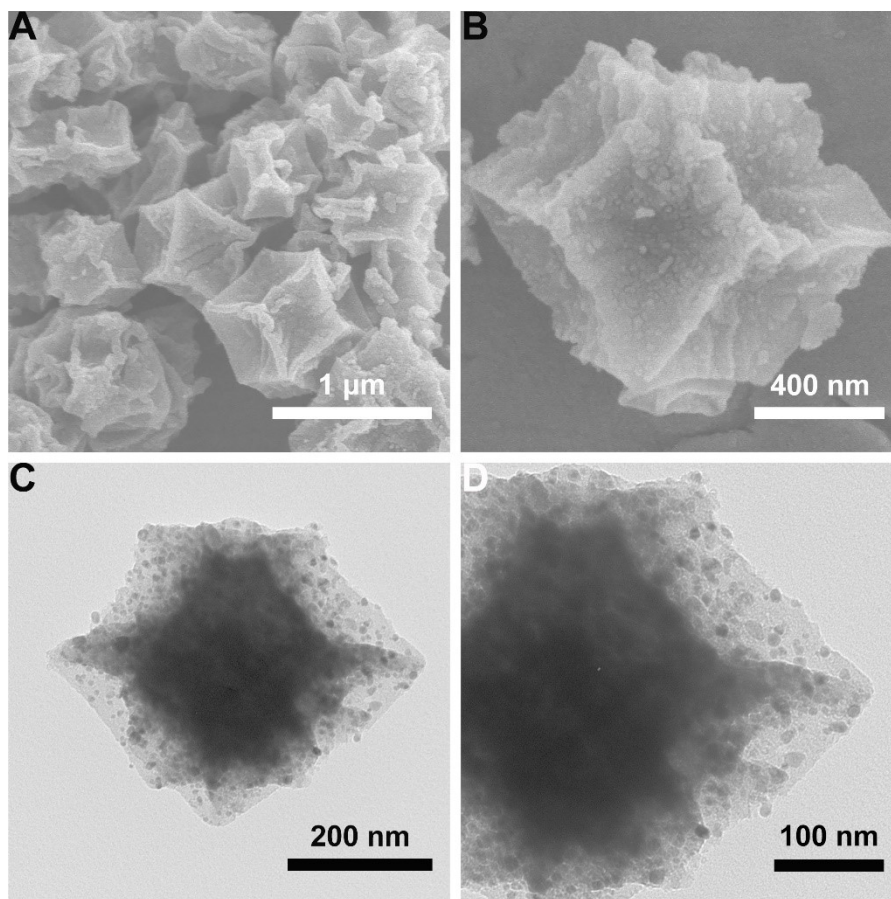


Fig. S7 (A-B) SEM and (C-D) TEM images of 3%Ce:Co-N-C.

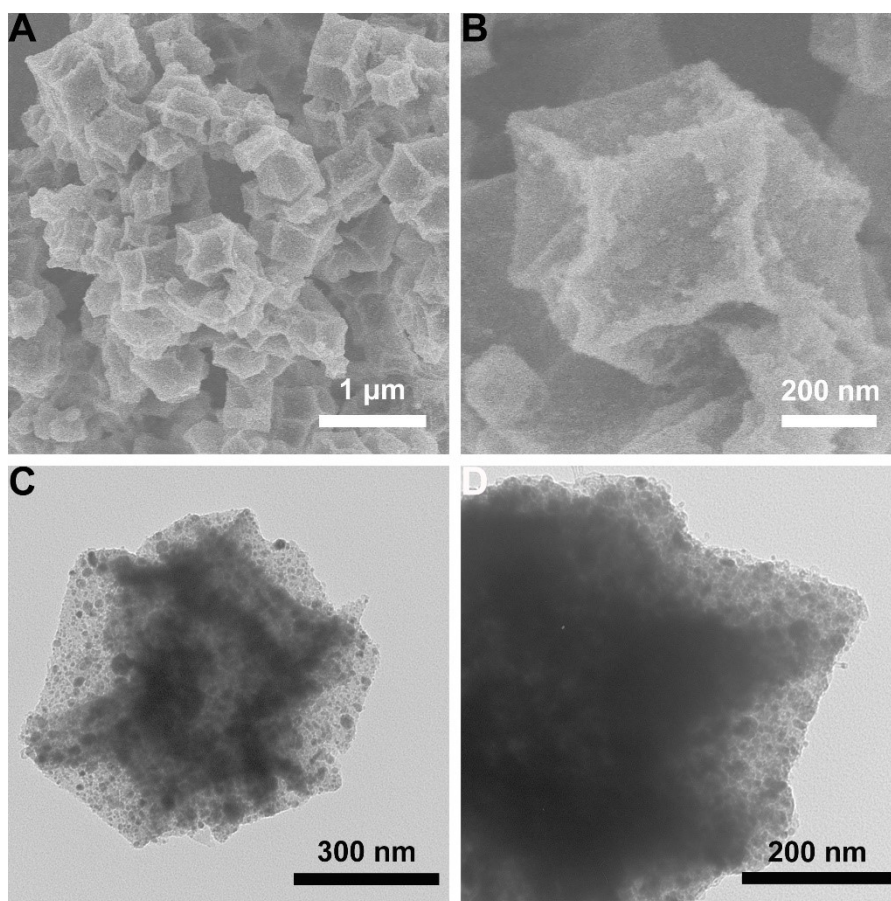


Fig. S8 (A-B) SEM and (C-D) TEM images of 5%Ce:Co-N-C.

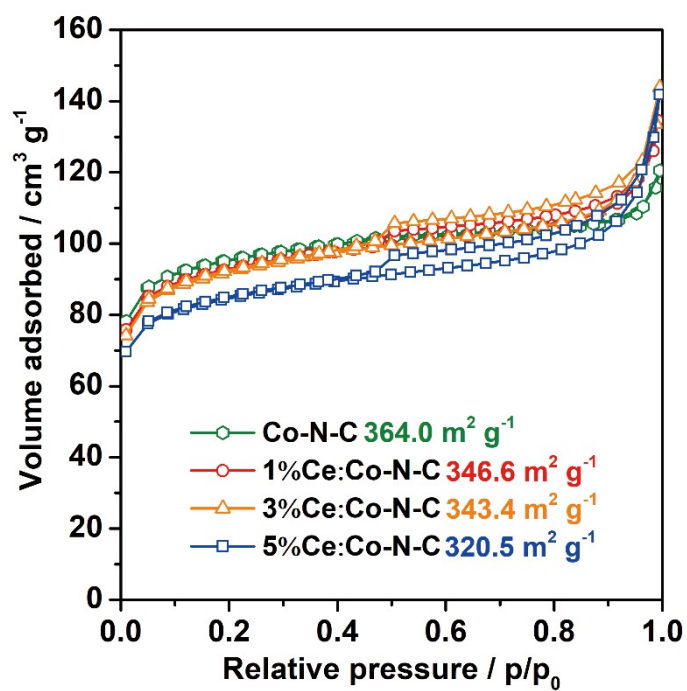


Fig. S9 Nitrogen adsorption/desorption isotherms with the BET specific surface area.

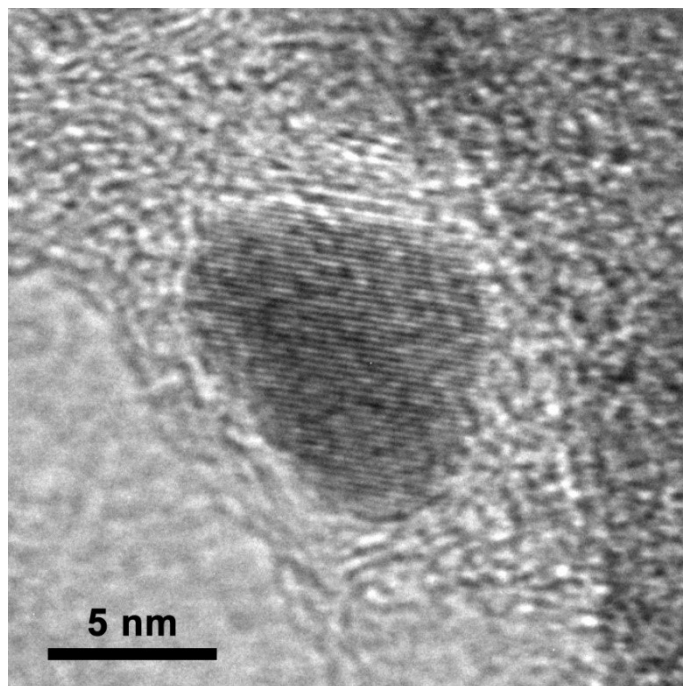


Fig. S10 HRTEM image of the pristine Co-N-C without Ce incorporation confirms the high crystallinity of the encapsulated Co nanocrystals without lattice disordering.

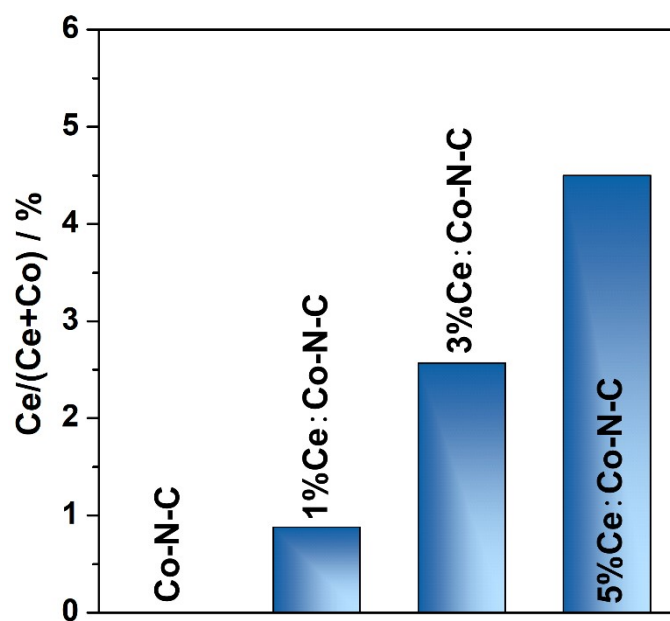


Fig. S11 ICP-OES data of the products. The Ce concentrations per total metals are 0.88%, 2.57% and 4.50% for 1%Ce:Co-N-C, 3%Ce:Co-N-C and 5%Ce:Co-N-C, respectively.

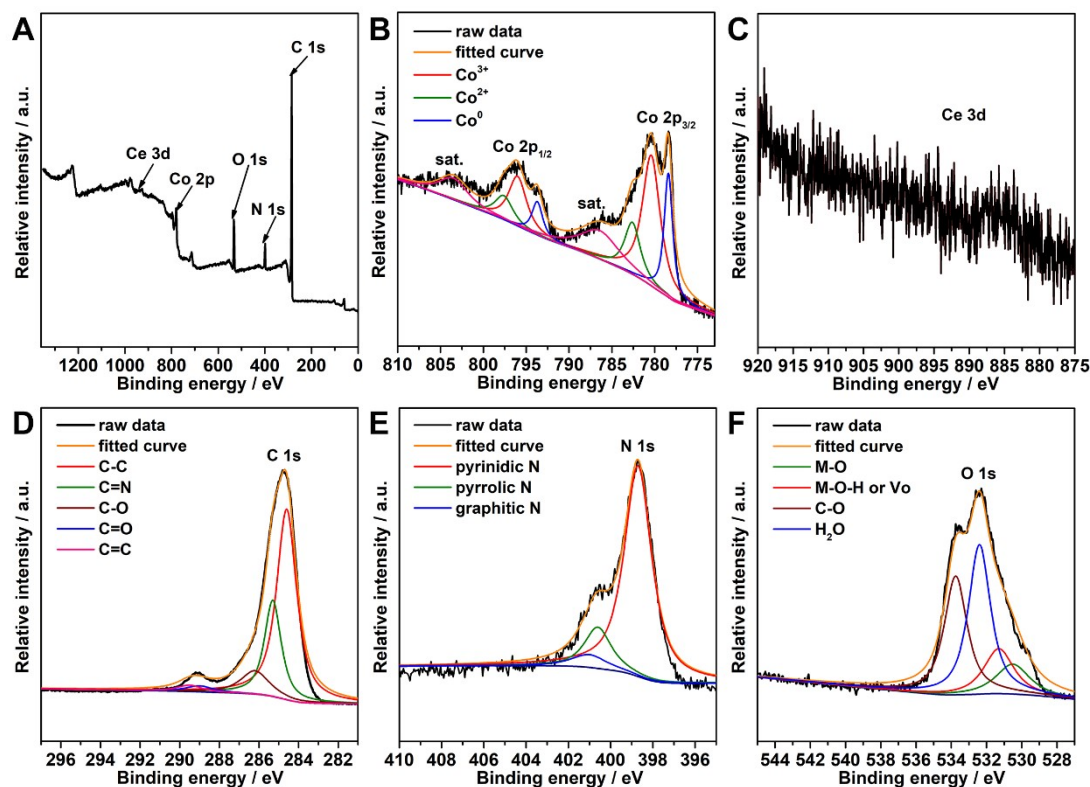


Fig. S12 (A) Survey spectrum and (B-F) XPS spectra of Co, Ce, C, N and O in 1%Ce:Co-N-C.

X-ray photoelectron spectroscopy (XPS) analyses were carried out to characterize the composition and valence of 1%Ce:Co-N-C (Fig. S12). As shown in Fig. S12A, the survey spectrum of 1%Ce:Co-N-C confirms the absence of contaminant elements besides Co, Ce, C, N and O. The Co 2p spectrum in Fig. S12B displays two major peaks assigned to the Co 2p_{3/2} and 2p_{1/2} orbitals. The deconvolution of Co 2p_{3/2} region shows triple peaks at 780.4, 782.7 and 778.4 eV, which can be ascribed to Co³⁺, Co²⁺ and Co⁰ species, respectively.¹⁻⁴ Similarly, the deconvoluted peaks at 796.0, 797.7 and 793.8 eV in Co 2p_{1/2} region can be attributed to Co³⁺, Co²⁺ and Co⁰ species. Therefore, abundant Co³⁺ and Co²⁺ ions can be identified in 1%Ce:Co-N-C besides metallic Co, which are located at the surface oxide nanolayers with disordered lattice. Of note, the XPS signal of Ce in Fig. S12C is too weak to be clearly identified owing to the low concentration of Ce below the sensitivity of XPS, while the content of Ce can be quantitatively measured by means of ICP-OES as indicated in Fig. S11. In

addition, the deconvolved C 1s peaks located at 284.6, 285.3, 286.2, 288.9 and 289.6 eV can be attributed to C-C, C=N, C-O, C=O and C=C, respectively,^{5,6} demonstrating the sp²-hybridized N-doped carbon skeleton with oxygen-containing groups (Fig. S12D). The XPS N 1s spectrum in Fig. S12E reveals three types of the nitrogen dopant, namely, pyridinic N (398.7 eV), pyrrolic N (400.6 eV) and graphitic N (401.1 eV),^{6,7} and the pyridinic N species are dominant in 1%Ce:Co-N-C. The nitrogen dopant in carbon support could facilitate the immobilization of the metal-based nanocrystals.^{3,8,9} That is, considering the strong interaction between Co/Ce ions and π electrons, the metal ions may preferentially aggregate on the sp²-type nitrogen sites and subsequently realize in situ nucleation and intimate anchoring of the metal/metal oxide nanocrystals. Moreover, more electrons can be injected into the carbon skeleton owing to the N doping, resulting in fast charge transport along the conductive substrate during HzOR.^{10,11} Furthermore, the O 1s spectrum can be deconvolved into four bands, corresponding to M-O bonds at 530.5 eV (M = Co or Ce), hydroxyl groups or oxygen vacancies at 531.3 eV, C-O bonds at 533.7 eV and adsorbed water at 532.3 eV (Fig. S12F),¹²⁻¹⁴ further verifying the formation of the oxide nanolayers induced by Ce incorporation.

Table S1 Comparison of the HzOR performance. The electrolyte is the mixed solution with 0.1 M KOH and 0.1 M hydrazine.

	Onset [V vs. RHE]	$j_{\text{geo}}@1.4\text{ V}$ vs. RHE [mA cm ⁻²]	Potential@ 10 mA cm ⁻² [V vs. RHE]	Stability	Ref.
1%Ce:Co-N-C	-0.05	55.8	0.225	104.3%@1000 cycles /94.5%@20 days	this work
Cu nanocluster/C	0.71	25.0	1.110	-	15
activated carbon	0.96	11.0	1.360	-	15
Fe ₂ MoC/N-C	0.35	-	0.570	~70%@2000 cycles	16
Ni nanoparticles	0.05	-	0.158	-	17
Ni/carbon black	0.05	-	-	-	17
O-rich MoS ₂	0.30	<1.0	-	49.8%@5000 s	18
flower-shaped CuO	0.789	~4.5	-	84.3%@3000 cycles /11%@1000 s	19

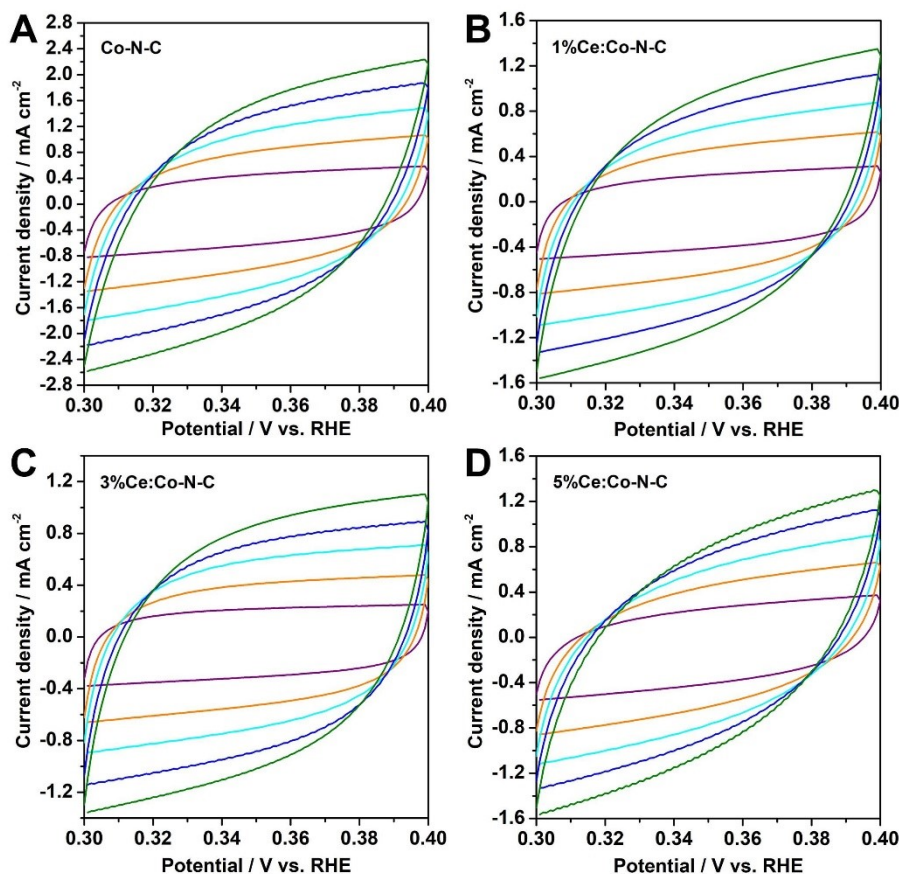


Fig. S13 (A-D) CV curves of the Co-based catalysts at non-redox region for the calculation of electrochemical double-layer capacitance.

The estimation of the effective active surface area of the samples was carried out according to literature.^{20, 21} Cyclic voltammetry (CV) was performed in O₂-degassed 0.1 M KOH solution at various scan rates (20, 40, 60, 80 and 100 mV s⁻¹) in 0.3-0.4 V vs. RHE region. The electrochemical double-layer capacitance (C_{dl}) of various samples can be determined from the cyclic voltammograms, which is expected to be linearly proportional to the effective surface area (Fig. S13). The double-layer capacitance is estimated by plotting the Δj ($j_{anode} - j_{cathode}$) at 0.35 V vs. RHE against the scan rate, where the slope is twice C_{dl} (Fig. 2C). The calculated values of double-layer capacitance are as follows: 14.1 mF cm⁻², 8.8 mF cm⁻², 8.5 mF cm⁻², and 7.1 mF cm⁻² for the pristine Co-N-C, 1%Ce:Co-N-C, 3%Ce:Co-N-C and 5%Ce:Co-N-C, respectively.

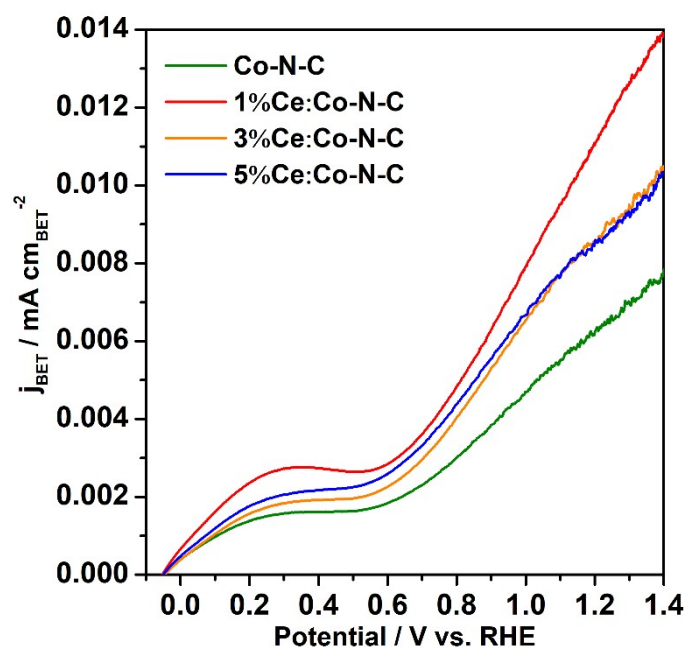


Fig. S14 LSV curves normalized by the BET specific surface areas of the catalysts.

Reference

1. J. Song, C. Zhu, B. Z. Xu, S. Fu, M. H. Engelhard, R. Ye, D. Du, S. P. Beckman and Y. Lin, *Adv. Energy Mater.*, 2017, **7**, 1601555.
2. I. S. Amiinu, X. Liu, Z. Pu, W. Li, Q. Li, J. Zhang, H. Tang, H. Zhang and S. Mu, *Adv. Funct. Mater.*, 2018, **28**, 1704638.
3. T. Wang, Z. Kou, S. Mu, J. Liu, D. He, I. S. Amiinu, W. Meng, K. Zhou, Z. Luo, S. Chaemchuen and F. Verpoort, *Adv. Funct. Mater.*, 2018, **28**, 1705048.
4. W. Liu, J. Xie, Y. Guo, S. Lou, L. Gao and B. Tang, *Journal of Materials Chemistry A*, 2019, **7**, 24437-24444.
5. B. Qiu, C. Yang, W. Guo, Y. Xu, Z. Liang, D. Ma and R. Zou, *J. Mater. Chem. A*, 2017, **5**, 8081-8086.
6. T. Liu, P. Zhao, X. Hua, W. Luo, S. Chen and G. Cheng, *J. Mater. Chem. A*, 2016, **4**, 11357-11364.
7. W. Zhang, X. Yao, S. Zhou, X. Li, L. Li, Z. Yu and L. Gu, *Small*, 2018, **14**, 1800423.
8. Y. Chen, S. Ji, Y. Wang, J. Dong, W. Chen, Z. Li, R. Shen, L. Zheng, Z. Zhuang, D. Wang and Y. Li, *Angew. Chem. Int. Ed.*, 2017, **56**, 6937-6941.

9. L. Gao, J. Xie, S. Liu, S. Lou, Z. Wei, X. Zhu and B. Tang, *ACS Appl. Mater. Interfaces*, 2020, **12**, 24701-24709.
10. A. L. Cazetta, T. Zhang, T. L. Silva, V. C. Almeida and T. Asefa, *Appl. Catal. B: Environ.*, 2018, **225**, 30-39.
11. L. Li, L. Song, H. Guo, W. Xia, C. Jiang, B. Gao, C. Wu, T. Wang and J. He, *Nanoscale*, 2019, **11**, 901-907.
12. J. Xie, H. Qu, F. Lei, X. Peng, W. Liu, L. Gao, P. Hao, G. Cui and B. Tang, *J. Mater. Chem. A*, 2018, **6**, 16121-16129.
13. J. Xie, S. Cao, L. Gao, F. Lei, P. Hao and B. Tang, *Chem. Commun.*, 2019, **55**, 9841-9844.
14. J. Xie, L. Gao, S. Cao, W. Liu, F. Lei, P. Hao, X. Xia and B. Tang, *J. Mater. Chem. A*, 2019, **7**, 13577-13584.
15. X. Gao, C. Du, C. Zhang and W. Chen, *ChemElectroChem*, 2016, **3**, 1266-1272.
16. K. Ojha, E. M. Farber, T. Y. Burshtein and D. Eisenberg, *Angew. Chem. Int. Ed.*, 2018, **57**, 17168-17172.
17. T.-Y. Jeon, M. Watanabe and K. Miyatake, *ACS Appl. Mater. Interfaces*, 2014, **6**, 18445-18449.
18. S. Song, Y. Li, Y. Shi, Y. Xu and Y. Niu, *J. Electroanal. Chem.*, 2022, **906**, 115986.
19. Y. Ma, H. Wang, J. Key, S. Ji, W. Lv and R. Wang, *J. Power Sources*, 2015, **300**, 344-350.
20. M. A. Lukowski, A. S. Daniel, F. Meng, A. Forticaux, L. Li and S. Jin, *J. Am. Chem. Soc.*, 2013, **135**, 10274-10277.
21. J. Xie, J. Zhang, S. Li, F. Grote, X. Zhang, H. Zhang, R. Wang, Y. Lei, B. Pan and Y. Xie, *J. Am. Chem. Soc.*, 2013, **135**, 17881-17888.